Langmuir

Article

pubs.acs.org/Langmuir

Toughness Governs the Rupture of the Interfacial H-Bond Assemblies at a Critical Length Scale in Hybrid Materials

Navid Sakhavand, Prakash Muthuramalingam, and Rouzbeh Shahsavari*

Department of Civil and Environmental Engineering, Rice University, Houston, Texas 77005, United States

Supporting Information

ABSTRACT: The geometry and material property mismatch across the interface of hybrid materials with dissimilar building blocks make it extremely difficult to fully understand the lateral chemical bonding processes and design nanocomposites with optimal performance. Here, we report a combined first-principles study, molecular dynamics modeling, and theoretical derivations to unravel the detailed mechanisms of H-bonding, deformation, load transfer, and failure at the interface of polyvinyl alcohol (PVA) and silicates, as an example of hybrid materials with geometry and property mismatch across the interface. We identify contributing H-bonds that are key to adhesion and demonstrate a specific periodic pattern of interfacial H-bond network dictated by the interface mismatch and intramolecular H-bonding. We find that the maximum toughness, incorporating both intra- and interlayer strain energy contributions, govern the existence of optimum overlap length and thus the rupture of interfacial (interlayer) H-bond assemblies in natural and synthetic hybrid materials. This universally valid result is in contrast to the previous reports that correlate shear strength with rupture of H-bonds assemblies at a finite overlap length. Overall, this work establishes a unified understanding to explain the interplay between geometric constraints, interfacial H-bonding, materials characteristics, and optimal mechanical properties in hybrid organic−inorganic materials.

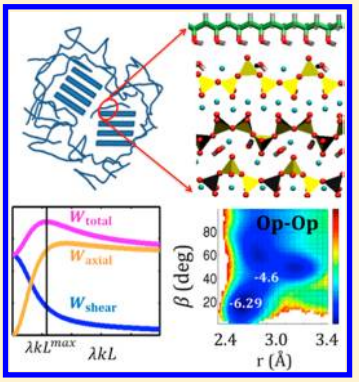

1. INTRODUCTION

By combining platelet-like ceramic building blocks and organic matrices nature creates hybrid materials such as bone, teeth and mollusk shells that have outstanding balance of stiffness, strength and flaw-tolerance.[1−3] This has inspired fabrication of several advanced human-made polymer−matrix composites with inorganic reinforcing materials such as cement, clays, glass, graphite, SiC, and mica.[4−7] In these hybrid materials, the adhesion and load transfer between organic and inorganic constituents at the nanoscale is a complex process that mainly trace back to the cooperative action of several chemical bonds. Considering hydrogen-bond (H-bond) network as the source of interfacial interactions, previous studies have primarily focused on either the average response of such hybrid materials under shear load, e.g., graphene oxide composite paper,[8,9] or the detailed processes of shear load transfer only between identical building blocks such as β-sheets in spider silk,[10−12] where the H-bond donor (guest) and the H-bond acceptor (host) sites for H-bonding are aligned in parallel. Despite the importance of the lateral H-bonding, there is currently no fundamental understanding (to our knowledge) on detailed mechanisms of interfacial interactions in hybrid materials where there is a mismatch between the guest and host sites across the interface.

To address this issue and illustrate our purpose, here we focus on synthetic polymer−silicates as a subclass of hybrid organic−inorganic materials and map out the inherent, nonintuitive characteristics of interfacial H-bonding and load transfer in these hybrid materials. A prime example of synthetic polymer−silicates is the introduction of polymers in calcium−silicate−hydrate (C−S−H) gel,[13−16] where the latter is the main product of cement hydration.[17] With Zeolitic-type pores and interlaminar distances of a few angstroms, C−S−H provides an excellent system to host polymers in confined spaces and study their hybrid chemical and physical behavior. Recent syntheses of various polymer C−S−H systems have shown enhanced material properties.[18−22] X-ray diffraction (XRD), nuclear magnetic resonance (NMR), and Fourier transform infrared spectroscopy (FTIR) experiments on polymer modified C−S−H reveal the intercalation of the polymer chains into the nanopores of the C−S−H.[19,23,24] There are reports on synthesized polymer modified C−S−H with several water-soluble polymers and incorporation of organic groups in C−S−H without disrupting its inorganic framework.[15,23] These experimental works suggested proximity of ethyl groups to the silica tetrahedra in C−S−H. Later, Mojumdar et al.[24] reported H-bonding between C−S−H and polyvinyl alcohol (PVA) by monitoring the shift in frequencies of FTIR spectra. In another study, the same group incorporated poly(acrylic acid) (PAA) into C−S−H[20] and reported intercalation of PAA as well as exfoliation of C−S−H. Their differential scanning calorimetry showed higher glass transition temperature of the hybrid material compared to the bulk

Received: April 15, 2013
Revised: May 24, 2013

   dx.doi.org/10.1021/la4014015 | Langmuir XXXX, XXX, XXX−XXX

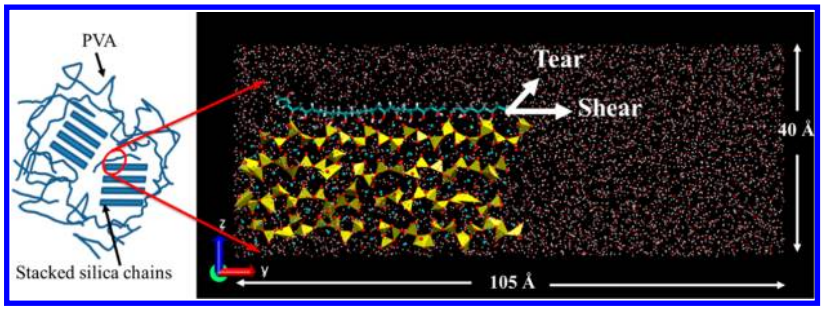

Figure 1. Closeup at the interface domain of PVA and tobermorite substrate. In the full atomic representation on the right, PVA chain is on the top and a silicate substrate (tobermorite) is at the bottom. The PVA and silicates are surrounded by water molecules in a periodic simulation box. In the shear mode, the polymer is dragged parallel to the silica chain of tobermorite while in the tear mode, it is pulled normal to the axis of silica chains.

polymer, thus suggesting potential applications in corrosive and high temperature environments.

It is widely hypothesized that in all polymer modified C−S−H nanocomposites the material property enhancements arise primarily from the H-bonding between polymers and the layered structure of the C−S−H gel.[13,24] However, the underlying chemistry and physics of these interactions and the mechanisms of load transfer between polymers and C−S−H remain elusive. The complexities originate from two major sources. First, polymers and C−S−H come from different chemistry classifications, thus unexpected characteristics can be found in their hybrid system which are absent in individual constituents.[25] The second source of complexity arises from the geometric anomaly between potential bonding agents at the interface of the two constituents, i.e., the short spacing distance between hydroxyl groups of PVA, $S_D \approx 2.15$ Å, compared to the longer spacing between silicon tetrahedra in the C−S−H substrate, $S_A \geq 7.5$ Å. Therefore, a basic understanding rooted in the subatomic level could provide important fundamental chemical insights to introduce new design concepts and principles for de novo synthesis of advanced hybrid materials.

Herein, we report a combined first-principles calculations, molecular dynamics (MD) modeling and theoretical study that together elucidate the binding characteristics at the interface of PVA and silica chains of tobermorite mineral, a natural analog of C−S−H.[17] Tobermorite has a layered structure with three repeating units of silicon tetrahedra where the third unit, so-called bridging silicon tetrahedron, is slightly shifted up or down (Figure 1). Here, as our main intention is to provide a fundamental insight, the simulations are set up based on the assumption of basal intercalation, where PVA strands interact with the interlayer tobermorite silica chains. The intercalation of polymers and C−S−H is a function of C/S ratio and type of the polymer.[22] It is known that in the absence of interlayer (basal) intercalation, the composite behavior of the C-SH and polymers will be similar to that in traditional composites.[24] However, interlayer intercalation of polymers in stacked nanocomposites is an important step to achieve enhanced material properties. Experimental measurements report no increase in basal spacing of PVA interaction with C−S−H for C/S < 1.[22] This suggests that interlayer intercalation of PVA does not occur for C−S−H with C/S <1, and thus interactions are intralayer in nature. However, with no reported experimental results for 1.1 nm tobermorite, the possibility of interlayer intercalation remains unknown. It must be noted that having intralayer or mixed intralayer−interlayer interactions adds more complexity to the environment.

First, by using potential mean force and time correlation function, we demonstrate that the H-bonding between hydroxyl groups of PVA and nonbridging oxygen atoms of silicate substrate are the primary source of adhesion at the interface of PVA−silicate system. Next, by pulling virtual experiments, we show that the effective resistance of the hybrid composite to fracture in shear mode is equivalent to fracture energy of approximately 2−6 H bonds. This finding translates into the existence of an optimum overlap length for which the toughness (total elastic strain energy density) of the composite is maximized. To provide critical mechanistic insights on the sources of such optimized overlap length in hybrid materials, a general theoretical model is developed and validated by an atomistic size-effect study. Finally, the detailed mechanism of interfacial H-bonding network between the PVA and silicate substrate is demonstrated that is dictated by the geometric anomaly at the interface and intramolecular H-bonding in PVA.

2. SYSTEM SETUP AND COMPUTATIONAL PROTOCOLS

2.1. MD Simulations. MD simulations were performed using a scalable parallel molecular dynamics simulator, LAMMPS.[26] The geometry of tobermorite crystal with a chemical formula of $Ca_6Si_6O_{18}.2H_2O$, was obtained from previous experimental work,[27] which includes 72 atoms per unit cell. The unit cell was then extended to a 1 × 7 × 1 supercell and relaxed with the CSH-FF potential.[28] This potential is an improved version of CLAYFF[29] potential and has been obtained by fitting to an extensive set of ab initio data on C−S−H family.[28] The ability of CSH-FF potential in accurately predicting the lattice parameters, bond distances, and other higher order properties of tobermorite and C−S−H has been previously validated against experiments or ab initio calculations.[28,30] Water molecules are modeled as the three-site simple point charge (SPC)[31] as described in CSH-FF. Partial charges and cutoffs and all parameters of CSH-FF potential are given in the Supporting Information (SI). The consistent valence force field (CVFF) potential[32] is employed as interatomic potential for PVA. CVFF is previously used in predicting hydrocarbon conformations and interface interactions.[33,34] The cross interaction terms between PVA and tobermorite are computed based on the standard Lorentz−Berthelot combination rules.[35]

To study the interaction of PVA with tobermorite, a single PVA chain is placed on top of a 1 × 7 × 1 supercell of tobermorite. The simulation was set up in this way to minimize the entropic effects of polymer conformations and focus on the mechanical characteristics of the interface. The PVA-tobermorite system is fully equilibrated in explicit water with approximate cell dimensions of 25 Å × 105 Å × 40 Å and periodic boundary conditions in all directions (Figure 1). These dimensions are chosen such that the PVA and tobermorite do not interact with their corresponding images. After relaxation, it turns out the parallel orientation of the PVA with silica chains is the favorable orientation. The built-in steered molecular dynamics (SMD) tool of

dx.doi.org/10.1021/la4014015 | Langmuir XXXX, XXX, XXX−XXX

LAMMPS was utilized to carry out the pulling virtual experiments. In our implementation, one end of a linear spring is tethered to the terminal carbon atom of the PVA, whereas the other end is pulled with a constant rate in either shear or tear direction, as shown in Figure 1. We used the spring constant of K = 10 kcal mol^{-1} Å^{-2} which has been previously used in similar computational conformations.[36] A full study on the effect of the pulling rate is detailed in section 3.2.

All MD relaxation and SMD simulations are performed under canonical ensemble (NVT) at 300 K with Nose-Hoover thermostat[37,38] for the time integration. The simulations have been relaxed for 2 ns with a time step of 1 fs and the trajectories are written out every 20 fs. To obtain the mechanisms of H-bonding, a PVA chain with 18 monomers is dragged by SMD simulations on tobermorite as shown in Figure 1.

2.2. DFT Calculations. The geometries of representative PVA−silicate complexes are optimized using density functional theory (DFT) with Becke's three-parameter hybrid functional combined with Lee−Yang−Parr correlation functional (B3LYP) with 6-31+G* and 6-311++G** basis sets.[39] The reliability of these methods in predicting the vibrational frequencies of H-bonded clusters is confirmed earlier.[40] The geometries of all clusters were optimized on their respective potential energy surfaces at the B3LYP/6-31+G* level of theory and atomic charge distributions are calculated from natural bond orbital (NBO) analysis at B3LYP/6-311++G** level of theory. Binding energies (BEs) of the complexes were calculated using the supermolecule approach and corrected for basis set superposition error (BSSE) using the counterpoise (CP) procedure.[41] Then, the BE is obtained via BE = $E_{complex} - (E_{pVA} + E_{tobermorite})$ where $E_{complex}$ is the total energy of the complex and E_{pVA} and $E_{tobermorite}$ are the PVA and tobermorite energies, respectively. All calculations were performed using the Gaussian 09.[42]

3. RESULTS AND DISCUSSION

3.1. Classification of Heterogeneous H-Bonds in the PVA-Silicate System. To obtain information on the influence of the H-bonds on the interface interactions, it is necessary to define them first. A hydrogen bond between a donor (D) and an acceptor (A) is usually defined based on the energetic and/or geometric criteria. A widely used geometric criterion for a H-bond symbolized by H−DA is when R < 3.5 Å and β < 30° where R represents the distance between D and A atoms, and β is the angle between the H−D and D−A rays.[43] While this criterion is suited to describe H-bonds that form in bulk water, to reduce arbitrariness in defining H-bonds in more complex systems such as PVA−tobermorite we adopt an energetic criterion based on two-dimensional (2D) potential of mean force (PMF).[44] In this method, for each 2D PMF plot that is constructed based on different choices of angles and distances, there is a lowest energy basin at short distances. This basin corresponds to the H-bonded states and is detached by a saddle point from another higher-energy basin that corresponds to the non-H-bonded states. Then, the equipotential contour that passes through the saddle point delineates the boundary for the H-bond. Mathematically, the PMF,$W(R,\beta)$, can be written as[44]

$$W_{HDA}(R, \beta) = -k_B T \ln(g_{HDA}(R, \beta)) \quad (1)$$

where k_B is the Boltzmann constant, T is temperature, and $g_{HDA}(R,\beta)$ is the angular-radial distribution function defining the probability of finding an acceptor atom (A) at the distance R from the donor (D) while forming an ADH angle of β. In the PVA−tobermorite composite there are four different types of oxygen atoms: the oxygen of PVA (Op), the bridging oxygen of silicates (Ob), the non-bridging oxygen of silicates (Onb), and the water oxygen (Ow). While all of these oxygen atoms can serve as H-bond acceptors, Op and Ow can also function as H-bond donors.

To obtain PMF plots, the PVA chain is initially located parallel to the silica chains with a distance more than a typical H-bond length to prevent initial H-bonding (Figure 2a). After

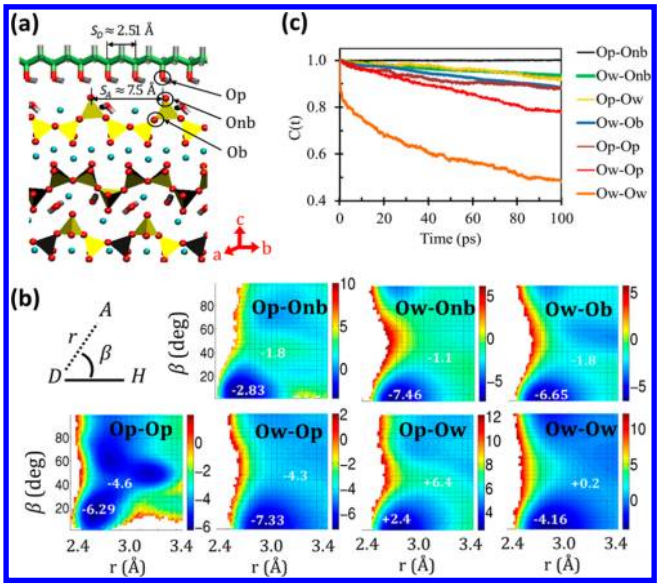

Figure 2. (a) Close-up atomistic snapshot of the PVA-tobermorite interface. Silicon tetrahedra are shown in yellow, oxygen atoms in red, calcium atoms in cyan, carbon atoms in green, and hydrogen atoms are shown in white. Op refers to oxygen of PVA, and Ob and Onb denote bridging and nonbridging oxygen atoms of silicates. (b) Potential of mean force plots for possible H-bonds in the PVA−tobermorite system calculated from MD simulations. The contours in the color bar are in units of k_BT. In all cases the magnitude of the global minima and the saddle points are shown with a white color. The inset on the top-left shows a schematic picture of a H-bond denoted by an acceptor (A), donor (D) and the hydrogen atom (H). (c) H-bond time correlation functions for different types of H-bonds. In the legend, the first and second atoms separated by the dash line indicate the donor and acceptor sites, respectively. Op denotes oxygen of PVA, Ow denotes oxygen of water, and Ob and Onb represent bridging and nonbridging oxygen atoms of silicates.

relaxation and investigating PMF plots for various pairs, it turns out there are only 7 types of H-bonds in our system, namely Op−Onb, Ow−Onb, Ow−Ob, Op−Op, Ow−Op, Op−Ow, and Ow−Ow. In all of these cases, the first symbols indicate the donor sites and the second symbols denote the acceptor sites. Figure 2b shows the PMF plots for these 7 cases calculated from MD simulations. The basins and saddle points are obvious in each PMF plot. To distinguish the heterogeneity of H-bonds strengths in the PVA−tobermorite system, we computed the intermittent H-bond Time correlation function (TCF)[30,43,45]

$$C(t) = \frac{\langle \delta n(t) \delta n(0) \rangle}{\langle \delta n(0) \delta n(0) \rangle} \quad (2)$$

where $n(t) = n(t) - \langle n \rangle$, and $n(t)$ is a binary operator representing H-bond population variable that takes the value of one if a pair of donor and acceptor are H-bonded, and zero otherwise. The symbol $\langle\rangle$ denotes average over all the pairs and time origins.[46] $C(t)$ is a representation of the number of the pairs which remain H-bonded since the assigned reference time. Thus, for a perfectly H-bonded pair, $C(t)$ remains nearly one over time whereas deviations from one indicate weak H-bond interactions.

dx.doi.org/10.1021/la4014015 | Langmuir XXXX, XXX, XXX−XXX

Considering H-bonds TCF in Figure 2c, the relaxation of the Op−Onb remains very slow even at long time scales, which indicates the high strength of this category of H-bonds. Note that Ow is in competence with Op to make H-bonds with Onb; however, Ow−Onb H-bond TCF decreases rapidly with time, indicating more favorable bonding between Op and Onb. Thus, we can conclude that Op−Onb H-bonds are the primary source of adhesion between PVA and silicates, serving as the load bearing points for load transfer between the organic and inorganic constituents of this hybrid composite.

While the interfacial H-bonding (Op−Onb) will be the primary focus of the present work, we can rank all of the hydrogen bonds from the strongest to the weakest as follows:

(1) Op−Onb (oxygen of PVA/nonbridging oxygen of silicates)
(2) Ow−Onb (water/nonbridging oxygen of silicates) and Op−Ow (oxygen of PVA/water)
(3) Op−Op (oxygen of PVA/oxygen of PVA) and Ow−Ob (water/bridging oxygen of silicates)
(4) Ow−Op (water/oxygen of PVA)
(5) Ow−Ow (water/water)

3.2. Efficient Number of H-Bonds Cross-Linking PVA and Silicates. To quantitatively study the load transfer at the PVA−silicate interface, SMD simulations are performed to impose incremental strains until fracture of the interface. For this purpose, a PVA with 12 mers is dragged on the surface of the tobermorite. The pulling virtual experiments include both shear and tear modes. In both cases the PVA chain is initially equilibrated and placed in parallel to the silicate chains. Next, via SMD simulation, the force is applied in parallel (perpendicular) to the silicate chains in the shear (tear) mode (see Figure 1). We use the tear mode to study single H-bonds since they break sequentially and use shear mode to study clusters of H-bonds as they break simultaneously.[10]

To compute the required energy for H-bond breakage in shear and tear modes, modified Bell's theory[47] is utilized, which is an extension of the conventional Bell model[48] to relate bond associated properties with the pulling speed. In the modified Bell's theory, the rupture force scales linearly with the logarithm of pulling velocity[10] (Figure 3):

$$F = \frac{k_B T}{x_b}\left(\ln v - \ln \frac{x_b}{\tau_0}\right) + \frac{E_b}{x_b} = a_1 \ln v - a_2 \tag{3}$$

$$a_1 = \frac{k_B T}{x_b},\quad a_2 = -\frac{k_B T}{x_b}\ln v_0,\quad v_0 = x_b/\tau_0 \exp\left(-\frac{E_b}{k_B T}\right) \tag{4}$$

In the above, τ_0 is the reciprocal of the natural frequency of bond oscillation, E_b is the bond energy, F is the maximum applied force, x_b is the bond extension required to initiate fracture,v is the pulling velocity,v_0 is the natural bond breaking speed, T is the temperature, and k_B is the Boltzmann constant as before. For each shear and tear mode, we simulated pulling virtual experiments with several velocities from 0.3 to 50 m/s consistent with previous studies.[49,50] Next, by line fitting for the two unknowns, a_1 and a_2, we calculated E_b and x_b (Figure 3b).

The energy barrier of the shear mode, E_b^{shear} = 6.33 kcal/mol, corresponds to the fracture energy of a cluster of H-bonds and the energy barrier of the tear mode, E_b^{tear} = 2.99 kcal/mol, corresponds to that for a single H-bond. Thus, the ratio of $E_b^{shear}/E_b^{tear} \approx 2.1$ indicates that an equivalent of nearly two H-bonds are broken simultaneously in the shear mode. In other words, under shear loading, regardless of how many H-bonds exist, the effective resistance to fracture is equivalent to fracture energy of a hybrid PVA−silicate system that is connected with ∼2.1 H-bonds. Considering that each H-bond donor (hydroxyl group) of PVA is linked with exactly one monomer, i.e., 1 H-bond = 1 monomer, this efficient number of H-bonds translates into an optimal overlap length that is critical for the shear load transfer and the overall mechanical performance of the composite. Considering the length of each monomer 2.51 Å, the modified Bell's theory suggest an optimum overlap distance of $L_{opt} \approx 5.3$ Å for the chosen system of PVA−tobermorite. The exact atomistic snapshots of H-bond assemblies before and after shear failure are discussed in section 3.5.

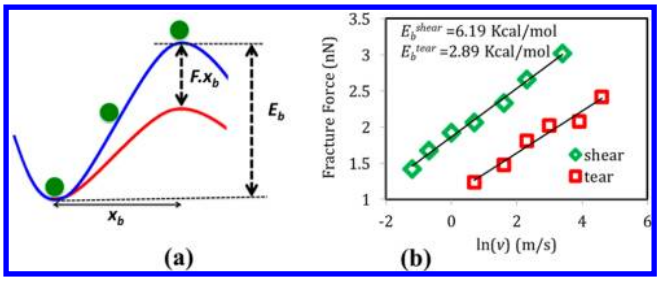

Figure 3. (a) Schematic profile of the energy barrier (E_b) and bond extension (X_b) between the equilibrium state and the transition state of an atomic bond. (b) SMD implementation of the modified Bell theory. The maximum forces for the shear and tear fracture modes are obtained as a function of the pulling speed, which after line-fitting result in estimation of energy barriers, E_b.

3.3. Shear Load Transfer between Dissimilar Building Blocks: Theoretical Model. In the previous section, the efficient number of H-bonds (overlap length) between the PVA and the silica chain was investigated via MD simulations and relevant theories. In this section, a theoretical-based model is proposed to reinforce the calculated overlap length and to provide more fundamental insights on the shear load transfer between the polymer and the silica chain. While the problem of shear load transfer between identical building blocks is studied within different contexts including adhesive lap joints[51] and staggered materials,[52−54] to our knowledge there is no study on the details of the optimum overlap length between dissimilar building blocks (here PVA and silica chains). To address this issue and to better understand the details of load transfer between PVA and silicate, we construct a simple 2D theoretical model to study shear lag between tablets with dissimilar properties and dimensions.

Assume two connected tablets with Young moduli, E_1 and E_2 and widths of b_1 and b_2 subjected to stress σ_0 on the right end of the top tablet (Figure 4a). Additionally, the system is clamped at the left end of the bottom tablet, and traction-free on all other dimensions except the overlap length, L. In our particular example, the top tablet denotes the PVA chain and the bottom tablet corresponds to the silica chain. The model also includes an intermediate layer (with thickness h), which models the interfacial H-bond layer between the PVA and the silica chains. The theoretical approach is derived in full detail in the Supporting Information (SI). We find that

dx.doi.org/10.1021/la4014015 | Langmuir XXXX, XXX, XXX−XXX

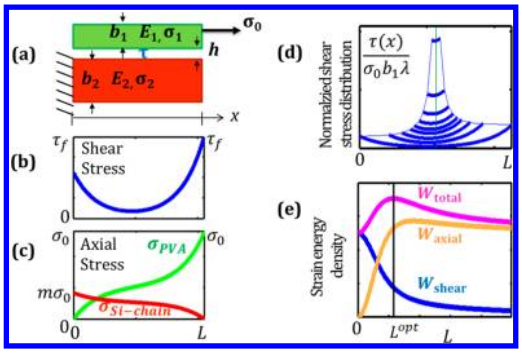

Figure 4. Analytical results of the elastic solution to the system of two dissimilar tablets under shear load interacting via a soft matrix. (a) Schematic view of the hybrid system where the top and bottom tablets represent PVA and Si-chain, respectively. (b) Typical shear stress distribution across the interface. (c) Typical axial stress distributions in the top and bottom tablets. (d) Normalized shear stress distribution as a function of varying overlap length. Note the higher values for shorter overlap length. (e) The behavior of total elastic strain energy density (toughness) and its shear and axial components as a function of the overlap length ($W_{total} = W_{axial} + W_{shear}$). At an optimum overlap length, the toughness W_{total} is maximized.

$$\sigma_1(x) = \frac{\sigma_0}{k^2}\left[\frac{\sinh(\lambda k x) - (k^2-1)\sinh(\lambda k(L-x))}{\sinh(\lambda k L)} + k^2 - 1\right]$$

$$\sigma_2(x) = \frac{-m\sigma_0}{k^2}\left[\frac{\sinh(\lambda k x) - (k^2-1)\sinh(\lambda k(L-x))}{\sinh(\lambda k L)} - 1\right]$$

$$\tau(x) = \frac{\lambda b_1 \sigma_0}{k}\left[\frac{\cosh(\lambda k x) + (k^2-1)\cosh(\lambda k(L-x))}{\sinh(\lambda k L)}\right] \quad (5a\text{–}c)$$

where

$$m = \frac{b_1}{b_2},\ n = \frac{E_1}{E_2},\ k^2 = mn + 1,\ \lambda^2 = \frac{G}{E_1 h b_1} \quad (6)$$

In the above, σ_1 and σ_2 are the axial stresses on the top and bottom tablets, τ is the shear stress between the two tablets, and G and h are the shear modulus and thickness of the interface, respectively. The elastic solutions expressed above are the generalized solution to the shear-lag problem of identical tablets and dimensions.[55−57] For the PVA parameters of b_1 = 3.3 Å, E_1 = 245 GPa,[58] and tobermorite parameters of b_2 = 11 Å, E_2 = 130 GPa,[59] (hence m = 0.3, n = 1.885) the typical axial and shear stress distributions are shown in Figure 4b,c. Compared to the two ends of the overlap length, the central region not carry much shear load, and thus is expected to contribute minimally to the overall strength of the hybrid system. Nonuniform but symmetric distribution of shear stress in staggered layer composites or shear lag models is known.[51,56,57] However, our model reveals that for dissimilar tablets shear stress distribution is not symmetric. In other words, not only the contribution of the interfacial H-bonds in the central region is negligible to the shear load transfer, but also those at the left end bear less shear stress compared to the H-bonds on the right end (Figure 4b). Note that while these behaviors may slightly change by choosing different estimates of E_1 and E_2 from the literature, the general trends of the plots in Figure 4 are unchanged.

To quantify influence of shear and axial stresses on rupture, we focus on the elastic strain energy density as it directly relates to the toughness and failure force. Toughness is a key material property that describes the ability of the material to absorb energy and deform without fracturing. For a material with a brittle interface failure such as PVA−silicate, the toughness is identical to the total elastic strain energy density, W_{total}. This parameter for the composite in Figure 4a can be written as (see the SI)

$$W_{total} = \frac{\tau_f^2}{G}\frac{h}{b_1 + b_2 + h} f(\lambda k L) \quad (7)$$

where

$$f(\lambda k L) = \frac{k^4 \coth(\lambda k L) + (k^2-1)\left(\lambda k L - 2\tanh\left(\frac{\lambda k L}{2}\right)\right)}{2\lambda k L(\coth(\lambda k L) + (k^2-1)\,\mathrm{csch}(\lambda k L))^2} \quad (8)$$

Equation 7 indicates that for fixed material properties of the composite, (E_1, E_2, and G) and constant thicknesses of the matrix and tablets (h, b_1, and b_2), i.e., constant m and k, the toughness is only the function of the overlap length, L. Thus, to maximize toughness, one has to maximize $f(\lambda k L)$. By using m = 0.3 and n = 1.885 for the PVA-tobermorite composite, the maximum of $f(\lambda k L)$ occurs at $\lambda k L_{opt} \approx 1.068$, suggesting an optimum overlap length of $L_{opt} \approx 0.854(E_1 h b_1/G)^{1/2}$ = 14.6 Å where h and G are taken 3 Å and G = 8.2 GPa, respectively (see the SI). Considering the approximate length of each PVA monomer 2.51 Å, this optimum overlap length of 14.6 Å yields $N_{opt} \approx 5.8$ as the optimum number of H-bonds (monomers), which is quite comparable with the modified Bell's theory predictions ($N_{opt} \approx 2.1$ and $L_{opt} \approx 5.3$ Å). Given the idealized nature of the 2D theoretical model compared to the atomistic simulation, this level of agreement in the order of magnitude is quite encouraging. The differences mainly arise from the complex processes that exist in the atomistic simulations but not accounted for in the theoretical model. These include the drag force of the surrounding water molecules on PVA in the pulling processes, various H-bonding between different species (as discussed in section 3.1) that may dynamically change the PVA adhesion to substrate and so on.

Figure 4d,e shows respectively the typical shear stress distribution, eq (5c), across the interface, and strain energy density (toughness) components obtained from the theoretical predictions as a function of the overlap length, L. It turns out that both the average shear stress, $\bar{\tau}$, as well as the shear component (W_{shear}) of the total strain energy density increase by decreasing L. These changes are even more pronounced for small overlaps where both $\tau(x)$ and W_{shear} approach their maximum values at the asymptotic limit of zero overlap length. However, at this extreme limit, the contribution of axial strain energy density W_{axial} (combined contributions from PVA and Si-chain) to total strain energy approaches zero. Thus, there is an optimum overlap length in which both shear and axial stresses offer their best contributions to maximize overall toughness W_{total} (Figure 4e). Note that the overlap length in which W_{total} is maximized is different than where W_{axial} is maximized. In our system, W_{axial} indicates contribution of intralayer bonds in both PVA and silicate layers to W_{total} while W_{shear} represents contribution of the interlayer H-bonds between PVA and silicates W_{total}. For a hybrid material with a brittle interface (linear elastic shear until failure) such as PVA−silicate, W_{total} reaches to its final value prior to failure. Thus, by varying the overlap length, one may find an optimum overlap length for which W_{total} is maximized preceding the interfacial

dx.doi.org/10.1021/la4014015 | Langmuir XXXX, XXX, XXX−XXX

failure. Note that here due to the stiff covalent C−C and Si−O bonds in PVA and silicates, upon pulling PVA on silicate substrate, mainly the angular C−C−C bond in PVA increase to accommodate the imposed intralayer stress. Our results show that the average C−C−C angle in PVA changes from ∼109° in equilibrium state to ∼112° preceding interfacial H-bond failure under shear mode.

Hence, although counterintuitive, at the optimum overlap length, the intralayer angular bonds in PVA and silicates slightly stretch to maximize overall toughness W_{total} preceding the interlayer (interfacial) H-bond failure. In fact, this is what the modified Bell's theory predicts from atomistic standpoint for brittle bond fracture. In such cases, the rupture force and maximum elastic strain energy density occur simultaneously. This analysis clearly explains the sources of the limited number of H-bonds (i.e., optimum overlap length) from the absorbed energy standpoints in the intra- and interlayer bonds. The fact that the results of this model only depend on intrinsic, "first-principles" properties of PVA and tobermorite and their geometry underlines the significance of our finding.

We can employ the elastic solution presented so far to infer about the failure force and the average interfacial shear strength of the hybrid material as a function of the overlap length. Considering that the brittle interface collapses at shear strength, $\tau_f = \tau(x = L)$, by rearranging eq (5c), one can obtain the failure force of the composite for a unit lateral length as

$$F = \frac{k\tau_f}{\lambda} \frac{1}{\coth(\lambda k L) + (k^2 - 1)\,\mathrm{csch}(\lambda k L)} \qquad (9)$$

This equation indicates that the failure force, F, initially increases with the overlap length and then becomes saturated. But the average interfacial shear strength, $\overline{\tau} = (F/L) = ((\int_0^L \tau(x)\,dx)/L)$, decrease with the overlap length. These two behaviors (not the magnitudes) are both independent of the choice of the material properties (E_1, E_2, G, τ_f) and dimensions (b_1, b_2, h). This rigorous theoretical derivation is strongly supported by an atomistic size-effect study described next.

3.4. Atomistic Size-Effect Study on the Influence of Overlap Length. We performed the size-effect study via SMD simulations by repeating the pulling virtual experiment in the shear mode for a PVA with chain lengths extending from one up to twelve monomers (Figure 5). The speed of pulling was fixed at 5×10^{-6} femtosecond/Å, consistent with previous studies.[36] To minimize the effects of initial configuration of PVA on the substrate, several simulations with different initial positions were conducted to obtain the average values of failure force from the first peak of force-displacement plots. Note that in the tear mode (the top-left panel in Figure 5), the pulling direction is out of the plane to break single H-bonds representing the failure force for a single mer.

Figure 6a,b represent respectively the failure force and the average interfacial shear strength obtained from the SMD simulations and theoretical model as a function of the number of monomers (overlap length). The trend obtained from the SMD simulations matches very well with our theoretical predictions. Together, they demonstrate that (i) the failure force of the composite initially increases linearly and then becomes saturated at an overlap length that is much larger than L^{opt} for which the toughness was optimized and (ii) the average interfacial shear strength monotonically increases by decreasing the overlap length. This latter finding obtained from rigorous mathematical modeling and a systematic size-effect study by atomistic simulations has a significant physical meaning: it elucidates that in contrast to the current understanding and

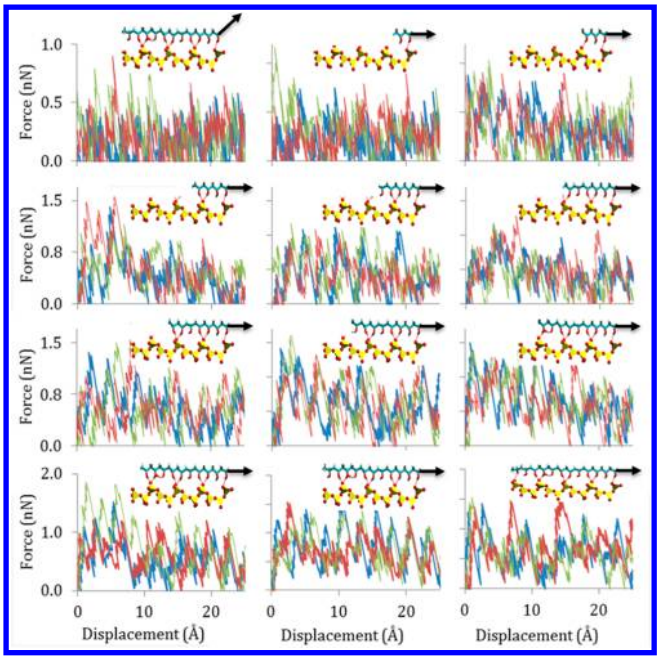

Figure 5. Atomistic size-effect study by SMD simulations to predict the failure force for different overlap lengths in PVA−silicate system. Twelve cases are considered representing overlap lengths of 1−12 mers. Note that in the top-left panel, the computational pulling is conducted out of the plane to break single H-bonds, i.e., tear mode. All other pulling experiments demonstrate the shear mode. The colors in each panel denote SDM results corresponding to different initial conditions.

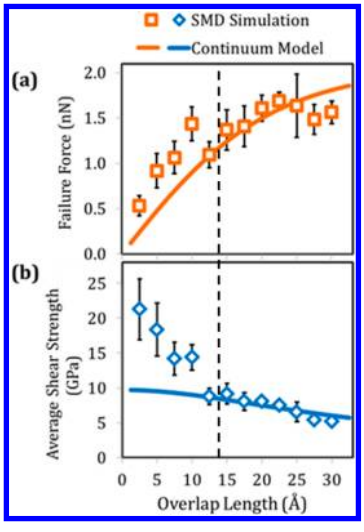

Figure 6. Failure force and the average interfacial shear strength of the hybrid material as a function of the overlap length (number of monomers). Both the theoretical model and the atomistic size-effect study show that the failure force increases monotonically as a function of the overlap length until it becomes saturated (a). The average interfacial shear strength is only maximized at the limit of zero overlap length (b). This confirms that unlike the earlier results in the literature (e.g., H-bonded β -sheet systems in proteins), the maximum shear strength cannot explain the sources of the optimum overlap length (see text). The vertical bars in panels a and b show the error bars in SMD simulations. The dashed line represents the location of the optimum toughness predicted by the continuum analysis.

dx.doi.org/10.1021/la4014015 | Langmuir XXXX, XXX, XXX−XXX

reports that correlate maximum "shear strength" with rupture of interfacial H-bonds assemblies at optimum overlap lengths, e.g., β-sheets in spider silks,[10−12] we find that the maximum toughness incorporating both axial (intralayer) and shear (interlayer) strain energy densities governs the rupture of interfacial H-bond assemblies at the optimum overlap length. This universally valid result, which is independent of the choice of natural or synthetic materials and geometric dimensions, is the most significant result of our paper. In the PVA−silicate system, the maximum toughness mainly comes from intralayer contributions (C−C−C angular bonds in PVA and Si−O−Si bonds in silicates) and interlayer H-bond contributions (Op−Onb H-bonds). It should be noted that the relatively large values of shear stress in Figure 6b is due to the very small overlap area (length of less than ∼30 Å, and unit lateral thickness) considered here. Nevertheless, the trends of the results are independent of the dimensions.

Note that an efficient overall load transfer occurs at an overlap length where the highest toughness and strength are met simultaneously. This is what happens in nature materials such as nacre, making them strong and tough concurrently. In the case of PVA−tobermorite, our continuum model predicts that toughness is maximized at $L_{opt} \approx 14.6$ Å while the strength will be asymptotically increasing with length. At $L_{opt} \approx 34.0$ Å the strength will reach 90% of its saturation value (see SI). Therefore, strength is optimized at an overlap length that is about 57% more than the length scale where toughness is maximized. Better efficiency can be achieved by tuning the tablet (tobermorite and/or PVA) and the interface (H-bonds) properties, e.g., use of another type of polymer such that the two length scale get closer. This will be discussed in detail in the future.

It is worthwhile to mention that our theoretical model is derived in a general framework that provides fundamental physical intuitions useful to understand, conceptualize and introduce new design concepts and principles for complex systems such as hybrid organic−inorganic materials with dissimilar building blocks.

3.5. Basic Mechanisms of H-Bonding at the PVA−Silicate Interface. The atomistic and theoretical results discussed so far provide the basic mechanistic insights on how H-bonding across the interface (particularly at the two ends) contributes to the load transfer and the optimized overlap length in hybrid materials. In this section, we unravel the detailed mechanisms of the H-bond rupture and formation that are key to load transfer at the interface of PVA and silica chains. The slip-stick behaviors of shear force versus displacement in Figure 5 indicate successive H-bond breakage and reformation. Additionally, the individual sudden force drops represent a brittle fracture behavior at the interface (although the overall sawtooth process may be viewed as a flaw-tolerant or may imply a deformation mode similar to those in metallic glasses[60] or glassy polymers[61]). As observed in a typical SMD simulation of Figure 5 (see the movie in the SI) and illustrated schematically in Figure 7, the distance between H-bond donor sites, S_D, and acceptor sites, S_A, are such that they dictate a certain H-bonding mechanism. Specifically, for every three adjacent hydroxyl groups of PVA (named as **1**, **2**, and **3**), two are H-bonded to a common acceptor site (Onb) in the substrate while the third one does not participate in any intermolecular H-bonding. Given such a geometric pattern, the detailed slip-stick processes in the PVA−silicate system include three basic mechanisms, which occur almost simultaneously.

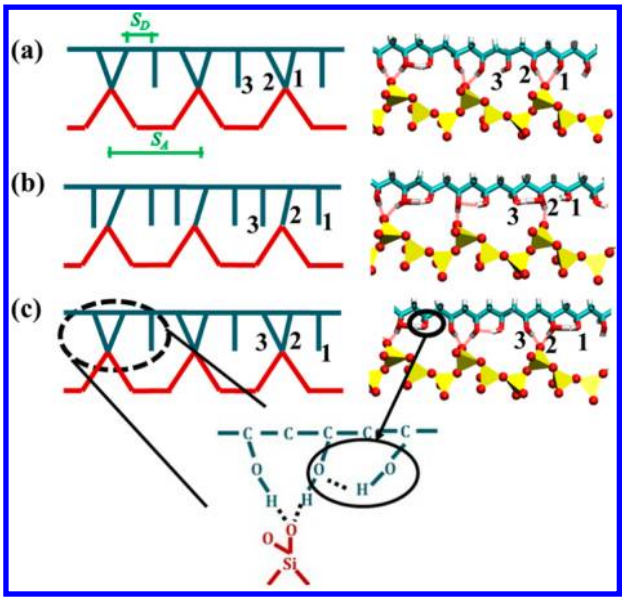

Figure 7. Detailed atomistic mechanisms of slip-stick processes between PVA and silicate substrate under shear force. (a-c) the schematic pictures on the left-hand side represent the intermolecular H-bonds shown on the right-hand side, obtained from the snapshots of SMD simulations. (a) PVA is shown on the top of the silica chain where two donor sites (two Op) share a common acceptor (Onb). On the left, each line in the PVA represents a hydroxyl group. (b) rupture of H-bond **1**, followed by reconfiguration of H-bond **2**. (c) The formation of a new H-bond **3** to recover the initial arrangement in panel a. The dashed black circle on the left highlights in the inter- and intramolecular H-bonding while the solid black circle on the right represent a typical intramolecular H-bonding in PVA. Flanked Si atoms of the substrate have two attached oxygen atoms but only one of them acts as a host site for intermolecular H-bonding to PVA (the other oxygen atom is out of plane and has a larger distance to the donor site). In panels b and c, red and white colors represent oxygen and hydrogen atoms while silicon and carbon atoms are shown with yellow and cyan colors. The dashed lines denote H-bonds.

The first mechanism is the breakage of H-bond **1**, which is immediately followed by (or concurrent with) the second mechanism, that is, shifting of H-bond **2** from an old alignment in Figure 7a to a new one in Figure 7c. This H-bond does not break during this reconfiguration. The third mechanism is the formation of a new H-bond **3**, which was not H-bonded previously and is formed in lieu of the broken H-bond **1** (Figure 7c).

While these basic mechanisms are identical for all the repeating units of the PVA−silicate interface, there are instances where local intramolecular H-bonding may significantly influence the interfacial properties. In particular, depending on the traveled distance of the PVA chains and the local environment, there might be intramolecular Op-Op H-bonding in the PVA. This is due to the mismatch distance between the donor and acceptor sites ($S_D \neq S_A$) at the interface. As shown in Figure 7c, the hydroxyl groups of the PVA chain, which cannot find any host at the silicate substrate, may form intramolecular H-bonds to acceptors within their own adjacent hydroxyl groups. To reveal the influence of these relatively strong H-bonds (see Figure 2c for comparison of H-bond strengths) that form within the PVA molecule on the interfacial mechanics of the hybrid PVA−silicate system, we performed first-principles calculations with high level of theory on small

dx.doi.org/10.1021/la4014015 | Langmuir XXXX, XXX, XXX−XXX

systems of PVA and silicon tetrahedra. Two cases were considered:

(1) a PVA with intramolecular H-bonding
(2) a PVA without intramolecular H-bonding.

In both cases, the PVAs interact with a silicon tetrahedron (Figure 8). Table 1 shows the calculated stretching frequency, intensity, red shift values and binding energies of the complexes for these two cases. Vibrational spectroscopy is a valuable tool to quantify the strength of weak H-bonding interactions in various complex materials. The free O−H stretching frequencies prior to complex formation in case 1 and 2 are 3655 and 3649 cm^{-1} and after the complex formation, these values change to 3277, and 3373 cm^{-1}, respectively. The calculated O−H frequency of case 1 is consistent with available experimental data,[62] i.e., 3250 cm^{-1}. The corresponding red shift and intensity values of Table 1 suggest that the case 1 has a better intermolecular connectivity than case 2. This can be verified from the calculated binding energy (BE) and electronegativity of atoms influencing the interfacial bonding (Figure 8). The BE of the complex in the case 1 is approximately 4 kcal/mol larger than that of in the case 2. Considering the electronegativity of atoms, before complex formation the charges on the oxygen atoms in PVA are less negative compared to those after complex formations. This reveals that electrons transfers from the Si−O bond to the H−O bond when a H-bond is formed. Particularly in case 1 (Figure 8b), due to the intramolecular H-bonding of PVA, the charge transfer is higher than that in the complex in case 2 (Figure 8d). This results in shorter H-bond distances and thus stronger intermolecular H-bonding across the interface. Interestingly, upon complex formation the intramolecular H-bonding of PVA, i.e., Op−Op, become shorter and stronger too (cf. Figure 8a,b).

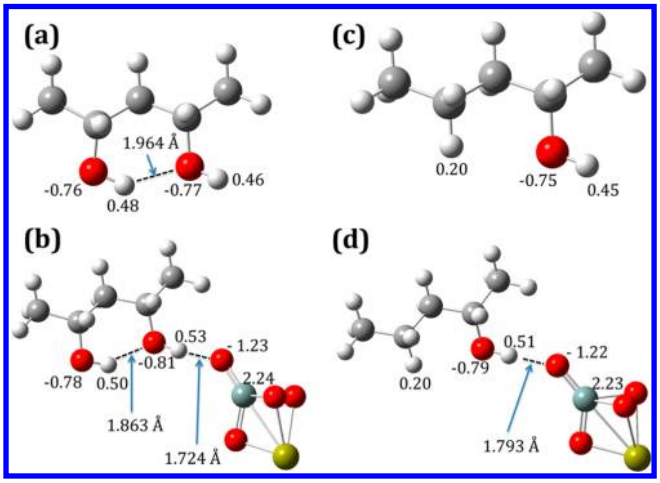

Figure 8. Panels a and b show optimized geometries and atomic charge distributions of a PVA with an intramolecular H-bond before and after complex formation with a silicon tetrahedron, respectively. For clarity only partial charges close to the interface are shown. Panels c and d show optimized geometries and atomic charge distributions of a PVA without an intramolecular H-bond before and complex formation with a silicon tetrahedron, respectively. For clarity only partial charges close to the interface are shown. The data are obtained from the B3LYP/6-311++G** level of theory. The gray, white, and red spheres represent carbon, hydrogen, and oxygen atoms, respectively, and orange and dark red denote silicon and calcium atoms. The calcium atoms are added to ensure charge neutrality.

Overall this analysis clearly elicits that intramolecular H-bonding in the PVA moiety, i.e., Op−Op, play a crucial role in the PVA−silicate complex formation and increase the strength of the intermolecular Op-Onb H-bonds across the interface. This suggests that the use of polymers with more intramolecular H-bonding may result in more interfacial adhesion, a feature that is not intuitive. This is particularly important for improving the synthetic brick-and-mortar composites (e.g., soft organic matrix with reinforcing inorganic platelets) discussed in section 1. Moreover, the first-principles analyses show that the PVA−silicate complexes are predominantly stabilized by the intermolecular H-bonds between PVA and silicates (Op−Onb), corroborating our results inferred from the PMF plots.

Finally, although PVA−silicate building blocks were used in this study as a platform to provide fundamental insights and quantitative mechanistic information on the interface interactions generated through a complex H-bond network, our findings have important implications on several other hybrid materials made of dissimilar building blocks in both natural and synthetic systems.

4. CONCUSIONS

In summary, we conducted a suite of DFT calculations, MD simulations, and theoretical methods to study the basic atomistic interactions, deformation mechanisms, and failure events of PVA−silicate systems, as an example of hybrid materials with geometric and material property mismatch across the interface. Our results reveal that the intermolecular H-bonding between PVA and the nonbridging oxygen atoms of the silicate substrate are the primarily source of adhesion and load transfer in such hybrid materials. This H-bond assembly has a certain periodic pattern controlled by the interfacial geometric anomaly. Specifically, due to the mismatch between successive donor and acceptor sites, for every three hydroxyl groups of PVA, two are H-bonded to a single acceptor site in

Table 1. Calculated O−H Stretching Frequencies, Red Shifts and Binding Energies of PVA−Silicate Complexes at B3LYP/6-31+G* Level of Theory, along with Available Experimental Value (cm^{-1})

PVA/silicate complex	O−H stretching	ν_{cal} (cm^{-1})	intensity	red shift (cm^{-1})	ν_{exp} (cm^{-1})	BEs (kcal/mol)
PVA	free O−H	3655	20			
case 1:	intramolecular H-bond	3581	157			
PVA−silicate	O−H···O_S	3277	1716	378	3250	14.47
	intramolecular H-bond	3460	273	121		(13.90)[a]
PVA	Free O−H	3649	20			
case 2:						
PVA−silicate	O−H···O_S	3373	1201	276		10.60 (9.73)

[a]BEs calculated at the B3LYP/6-311++G** level.

dx.doi.org/10.1021/la4014015 | Langmuir XXXX, XXX, XXX−XXX

silicate substrate while the third hydroxyl group is left nonbonded. However, depending on the applied force and local environment, these stand alone hydroxyl groups may form intramolecular H-bonding within PVA, which then entail nonintuitive consequences: intramolecular H-bonding within PVA increases the electronegativity of atoms that are participating in the intermolecular H-bonding, thus resulting in larger binding energy and adhesion across the interface. The latter suggests that depending on the frequency of host-sites, the use of polymers with the possibility of more intramolecular H-bonding may result in better mechanical adhesion to the substrate. This is particularly important for improving the connectivity of synthetic brick-and-mortar composites (e.g., inorganic reinforcing platelets embedded in a soft organic matrix).

More importantly, we developed a general theoretical model that formulated the deformation of two dissimilar tablets connected by a soft matrix. By linking the results of modified Bell's theory and theoretical derivations, we find that the maximum toughness, incorporating both axial (intralayer) and shear (interlayer) strain energy contributions, governs the existence of optimum overlap length and thus the rupture of interfacial H-bond assemblies in natural and synthetic materials. This universally valid result is in contrast to the current understanding and reports that correlate "shear strength" with rupture of H-bonds assemblies at optimum length scales.[10−12] We demonstrated that at the optimum overlap length, the intralayer bonds in the tablets slightly stretch to maximize toughness W_{total} preceding the interlayer (interfacial) H-bond failure. The developed theoretical model is not limited to the PVA−silicate materials and can be used for numerous organic, inorganic or hybrid materials.

Our results may lay the foundation for the development of new "unit processes" that govern the rupture of hybrid organic−inorganic materials. A rich set of models for the deformation and fracture of ceramics and metallic systems have been developed over the past decades, describing dislocations, shear bands, and plasticity. However, similar advances for hybrid organic−inorganic materials, especially at their interface which is often the roadblock for improving the material properties, have thus far remained elusive. In analogy to dislocation nucleation and propagation in metals or shear band in metallic glasses, the breaking of interfacial H-bonds across the interface represents a basic unit process of failure in hybrid organic−inorganic materials. To the best of our knowledge, this report for the first time describes a rigorous holistic approach integrating DFT calculations, MD simulations, size-effect study, and theoretical methods to describe the fundamental deformation mechanisms and interfacial H-bond failure events in hybrid organic−inorganic materials.

■ ASSOCIATED CONTENT

Supporting Information

Complete derivation of the theoretical model, extraction of shear modulus (G), and maximum shear strength (τ_f), CSH-FF force field potential parameters, a 2 ns movie of SMD simulation of pulling PVA on silicate substrate representing the slip-stick motions. In the movie, the successive breakage and formation of H-bond assemblies are clearly visible. This material is available free of charge via the Internet at http://pubs.acs.org.

■ AUTHOR INFORMATION

Corresponding Author

*E-mail: rouzbeh@rice.edu.

Notes

The authors declare no competing financial interest.

■ ACKNOWLEDGMENTS

The financial support by Rice University is greatly acknowledged. The supercomputer machines utilized in this work were supported in part by NIH award NCRR S10RR02950 and an IBM Shared University Research (SUR) Award in partnership with CISCO, Qlogic and Adaptive Computing, and in part by the Data Analysis and Visualization Cyber infrastructure funded by NSF under grant OCI-0959097.

■ REFERENCES

(1) Espinosa, H. D.; Rim, J. E.; Barthelat, F.; Buehler, M. J. Merger of structure and material in nacre and bone − Perspectives on de novo biomimetic materials. *Prog. Mater. Sci.* **2009**, *54* (8), 1059−1100.

(2) Fratzl, P.; Burgert, I.; Gupta, H. S. On the role of interface polymers for the mechanics of natural polymeric composites. *Phys. Chem. Chem. Phys.* **2004**, *6* (24), 5575−5579.

(3) Gao, H. Application of Fracture Mechanics Concepts to Hierarchical Biomechanics of Bone and Bone-like Materials. *Int. J. Fract.* **2006**, *138* (1−4), 101−137.

(4) Beaudoin, J.; Dramé, H.; Raki, L.; Alizadeh, R. Formation and properties of C-S-H−PEG nano-structures. *Mater. Struct.* **2009**, *42* (7), 1003−1014.

(5) Bonderer, L. J.; Studart, A. R.; Gauckler, L. J. Bioinspired Design and Assembly of Platelet Reinforced Polymer Films. *Science* **2008**, *319* (5866), 1069−1073.

(6) Rexer, J.; Anderson, E. Composites with planar reinforcements (flakes, ribbons)—A review. *Polym. Eng. Sci.* **1979**, *19* (1), 1−11.

(7) Tang, Z.; Kotov, N. A.; Magonov, S.; Ozturk, B. Nanostructured artificial nacre. *Nat. Mater.* **2003**, *2* (6), 413−418.

(8) Medhekar, N. V.; Ramasubramaniam, A.; Ruoff, R. S.; Shenoy, V. B. Hydrogen Bond Networks in Graphene Oxide Composite Paper: Structure and Mechanical Properties. *ACS Nano* **2010**, *4* (4), 2300−2306.

(9) Compton, O. C.; Cranford, S. W.; Putz, K. W.; An, Z.; Brinson, L. C.; Buehler, M. J.; Nguyen, S. T. Tuning the Mechanical Properties of Graphene Oxide Paper and Its Associated Polymer Nanocomposites by Controlling Cooperative Intersheet Hydrogen Bonding. *ACS Nano* **2011**, *6* (3), 2008−2019.

(10) Keten, S.; Buehler, M. J. Geometric Confinement Governs the Rupture Strength of H-bond Assemblies at a Critical Length Scale. *Nano Lett.* **2008**, *8* (2), 743−748.

(11) Keten, S.; Buehler, M. J. Strength limit of entropic elasticity in beta-sheet protein domains. *Phys. Rev. E* **2008**, *78* (6), 061913.

(12) Keten, S.; Xu, Z.; Ihle, B.; Buehler, M. J. Nanoconfinement controls stiffness, strength and mechanical toughness of [beta]-sheet crystals in silk. *Nat. Mater.* **2010**, *9* (4), 359−367.

(13) Beaudoin, J. J.; Raki, L.; Alizadeh, R. A 29Si MAS NMR study of modified C−S−H nanostructures. *Cement Concrete Composites* **2009**, *31* (8), 585−590.

(14) Matsuyama, H.; Young, J. F. Synthesis of calcium silicate hydrate/polymer complexes: Part I. Anionic and nonionic polymers. *J. Mater. Res.* **1999**, *14* (8), 10.

(15) Minet, J.; Abramson, S.; Bresson, B.; Franceschini, A.; Van Damme, H.; Lequeux, N. Organic calcium silicate hydrate hybrids: a new approach to cement based nanocomposites. *J. Mater. Chem.* **2006**, *16* (14), 1379−1383.

(16) Pellenq, R. J.-M.; Lequeux, N.; Van Damme, H. Engineering the bonding scheme in C-S-H: The iono-covalent framework. *Cem. Concr. Res.* **2008**, *38*, 159−174.

(17) Taylor, H. F. W. Proposed Structure for Calcium Silicate Hydrate Gel. *J. Am. Ceram. Soc.* **1986**, *69* (6), 464−467.

(18) Alizadeh, R. *Nanostructure and engineering properties of basic and modified calcium-silicate-hydrate systems*: University of Ottawa: Ottawa, 2009.
(19) Okamoto, M. *Polymer/layered silicate nonmcomposites*; Rapra Technology Ltd.: 2003; p 166.
(20) Mojumdar, S. C.; Raki, L. Synthesis, thermal and structural characterization of nanocomposites for potential applications in construction. *J. Therm. Anal. Calorim.* **2006**, *86* (3), 651−657.
(21) Sinha Ray, S.; Okamoto, M. Polymer/layered silicate nanocomposites: a review from preparation to processing. *Prog. Polym. Sci.* **2003**, *28* (11), 1539−1641.
(22) Matsuyama, H.; Young, J. F. Intercalation of Polymers in Calcium Silicate Hydrate: A New Synthetic Approach to Biocomposites? *Chem. Mater.* **1998**, *11* (1), 16−19.
(23) Merlin, F.; Lombois, H.; Joly, S.; Lequeux, N.; Halary, J.-L.; Van Damme, H. , Cement-polymer and clay-polymer nano- and mesocomposites: spotting the difference. *J. Mater. Chem.* **2002**, *12* (11), 3308−3315.
(24) Mojumdar, S. C.; Raki, L., Characterization and properties of calcium silicate hydrate polymer nanocomposites. In *Proceedings of The American Ceramic Society 107th Annual Meeting*, 2005; pp 1−10.
(25) Chujo, Y. Organic-Inorganic Nano-Hybrid Materials. *Kona* **2007**, *25*, 255−260.
(26) Plimpton, S. Fast Parallel Algorithms for Short-Range Molecular Dynamics. *J. Comput. Phys.* **1995**, *117* (1), 1−19.
(27) Hamid, S. A. The crystal structure of the 11Å natural tobermorite Ca2.25[Si3O7.5(OH)1.5]·1H2O. *Z. Kristallogr.* **1981**, *154* (3−4), 189−198.
(28) Shahsavari, R.; Pellenq, R. J. M.; Ulm, F.-J. Empirical force fields for complex hydrated calcio-silicate layered materials. *Phys. Chem. Chem. Phys.* **2011**, *13* (3), 1002−1011.
(29) Cygan, R. T.; Liang, J.-J.; Kalinichev, A. G. Molecular Models of Hydroxide, Oxyhydroxide, and Clay Phases and the Development of a General Force Field. *J. Phys. Chem. B* **2004**, *108* (4), 1255−1266.
(30) Youssef, M.; Pellenq, R. J. M.; Yildiz, B. Glassy Nature of Water in an Ultraconfining Disordered Material: The Case of Calcium−Silicate−Hydrate. *J. Am. Chem. Soc.* **2011**, *133* (8), 2499−2510.
(31) Teleman, O.; Jönsson, B.; Engström, S. A molecular dynamics simulation of a water model with intramolecular degrees of freedom. *Mol. Phys.* **1987**, *60* (1), 193−203.
(32) Cornell, W. D.; Cieplak, P.; Bayly, C. I.; Gould, I. R.; Merz, K. M.; Ferguson, D. M.; Spellmeyer, D. C.; Fox, T.; Caldwell, J. W.; Kollman, P. A. A Second Generation Force Field for the Simulation of Proteins, Nucleic Acids, and Organic Molecules. *J. Am. Chem. Soc.* **1995**, *117* (19), 5179−5197.
(33) Asensio, J. L.; Martin-Pastor, M.; Jimenez-Barbero, J. The use of CVFF and CFF91 force fields in conformational analysis of carbohydrate molecules. Comparison with AMBER molecular mechanics and dynamics calculations for methyl α-lactoside. *Int. J. Biol. Macromol.* **1995**, *17* (3−4), 137−148.
(34) Raffaini, G.; Ganazzoli, F. Sequential adsorption of proteins and the surface modification of biomaterials: A molecular dynamics study. *J. Mater. Sci.: Mater. Med.* **2007**, *18* (2), 309−316.
(35) Hansen, J.; McDonald, I. R. *Theory of Simple Liquids*; Academic Press: New York, 1986.
(36) Sotomayor, M.; Schulten, K. Single-Molecule Experiments in Vitro and in Silico. *Science* **2007**, *316* (5828), 1144−1148.
(37) Hoover, W. G. Canonical dynamics: Equilibrium phase-space distributions. *Phys. Rev. A* **1985**, *31* (3), 1695−1697.
(38) Nose, S. A unified formulation of the constant temperature molecular dynamics methods. *J. Chem. Phys.* **1984**, *81* (1), 511−519.
(39) Parr, R. G. Y. *Density-Functional Theory of Atoms and Molecules*; Oxford University Press: Oxford, U.K., 1994.
(40) Prakash, M.; Subramanian, V. Structure, stability and spectral signatures of monoprotic carborane acid-water clusters (CBWn, where n = 1−6). *Phys. Chem. Chem. Phys.* **2011**, *13* (48), 21479−21486.
(41) Boys, S. F.; Bernardi, F. The calculation of small molecular interactions by the differences of separate total energies. Some procedures with reduced errors. *Mol. Phys.* **1970**, *19* (4), 553−566.
(42) Frisch, M. J.; et al. Gaussian 09, revision A.1; Gaussian, Inc.: Wallingford, CT, 2009.
(43) Luzar, A.; Chandler, D. Hydrogen-bond kinetics in liquid water. *Nature* **1996**, *379* (6560), 55−57.
(44) Kumar, R.; Schmidt, J. R.; Skinner, J. L. Hydrogen bonding definitions and dynamics in liquid water. *J. Chem. Phys.* **2007**, *126* (20), 204107−12.
(45) Pal, S.; Bandyopadhyay, S. Importance of Protein Conformational Motions and Electrostatic Anchoring Sites on the Dynamics and Hydrogen Bond Properties of Hydration Water. *Langmuir* **2013**, *29* (4), 1162−1173.
(46) Haile, J. M. *Molecular Dynamics Simulation*; John Wiley & Sons, Inc.: New York, 1992.
(47) Ackbarow, T.; Chen, X.; Keten, S.; Buehler, M. J. Hierarchies, Multiple Energy Barriers, and Robustness Govern the Fracture Mechanics of α-Helical and β-Sheet Protein Domains. *Proc. Natl. Acad. Sci. U.S.A.* **2007**, *104* (42), 16410−16415.
(48) Bell, G. I. Models for the specific adhesion of cells to cells. *Science* **1978**, *200* (4342), 618−627.
(49) Lu, H.; Schulten, K. The Key Event in Force-Induced Unfolding of Titin's Immunoglobulin Domains. *Biophys. J.* **2000**, *79* (1), 51−65.
(50) Gao, M.; Craig, D.; Lequin, O.; Campbell, I. D.; Vogel, V.; Schulten, K. Structure and functional significance of mechanically unfolded fibronectin type III1 intermediates. *Proc. Natl. Acad. Sci.* **2003**, *100* (25), 14784−14789.
(51) Volkersen, O. Die Nietkraftverteilung in zugbeanspruchten Nietverbindungen mit konstantin Lenschenquerschnit. *Luftfahrtforschung* **1938**, *15*, 41−47.
(52) Beyerlein, I. J.; Landis, C. M. Shear-lag model for failure simulations of unidirectional fiber composites including matrix stiffness. *Mech. Mater.* **1999**, *31* (5), 331−350.
(53) Jäger, I.; Fratzl, P. Mineralized Collagen Fibrils: A Mechanical Model with a Staggered Arrangement of Mineral Particles. *Biophys. J.* **2000**, *79* (4), 1737−1746.
(54) Nairn, J. A. On the use of shear-lag methods for analysis of stress transfer in unidirectional composites. *Mech. Mater.* **1997**, *26* (2), 63−80.
(55) Chen, B.; Wu, P. D.; Gao, H. A characteristic length for stress transfer in the nanostructure of biological composites. *Compos. Sci. Technol.* **2009**, *69* (7−8), 1160−1164.
(56) Liu, Y.; Xie, B.; Zhang, Z.; Zheng, Q.; Xu, Z. Mechanical properties of graphene papers. *J. Mech. Phys. Solids* **2012**, *60* (4), 591−605.
(57) Wei, X.; Naraghi, M.; Espinosa, H. D. Optimal Length Scales Emerging from Shear Load Transfer in Natural Materials: Application to Carbon-Based Nanocomposite Design. *ACS Nano* **2012**, *6* (3), 2333−44.
(58) Sakurada, I.; Kaji, K.; Nakamae, K.; Wadano, S. Experimental Determination of the Elastic Moduli of Polymer Crystals in the Direction Perpendicular to the Chain Axis. *Bull. Inst. Chem. Res.* **1966**, *44*, 2.
(59) Shahsavari, R.; Buehler, M. J.; Pellenq, R. J. M.; Ulm, F.-J. First-Principles Study of Elastic Constants and Interlayer Interactions of Complex Hydrated Oxides: Case Study of Tobermorite and Jennite. *J. Am. Ceram. Soc.* **2009**, *92* (10), 2323−2330.
(60) Argon, A. S.; Demkowicz, M. J. What Can Plasticity of Amorphous Silicon Tell Us about Plasticity of Metallic Glasses? *Metall. Mater. Trans. A* **2008**, *39* (8), 1762−1778.
(61) Mott, P. H.; Argon, A. S.; Suter, U. W. Atomistic modelling of cavitation of glassy polymers. *Philos. Mag. A* **1993**, *68* (3), 537−564.
(62) Yu, Y. H.; Lin, C. Y.; Yeh, J. M.; Lin, W. H. Preparation and properties of poly(vinyl alcohol)-clay nanocomposite materials. *Polymer* **2003**, *44* (12), 3553−3560.

dx.doi.org/10.1021/la4014015 | *Langmuir* XXXX, XXX, XXX−XXX